

Reconstruction of the wave functions of coupled nanoscopic emitters using a coherent optical technique

Marten Richter,^{1,2,*} Felix Schlosser,¹ Mario Schoth,¹ Sven Burger,³ Frank Schmidt,³ Andreas Knorr,¹ and Shaul Mukamel²

¹*Institut für Theoretische Physik, Nichtlineare Optik und Quantenelektronik, Technische Universität Berlin, Hardenbergstr. 36, 10623 Berlin, Germany*

²*Department of Chemistry, University of California, Irvine, California 92697-2025, USA*

³*Zuse Institute Berlin, Takustr. 7, 14195 Berlin, Germany*

(Received 17 January 2012; revised manuscript received 9 July 2012; published 10 August 2012)

We show how coherent, spatially resolved spectroscopy can disentangle complex hybrid wave functions into wave functions of the individual emitters. This way, detailed information on the coupling of the individual emitters, not available in far-field spectroscopy, can be revealed. Here we propose a quantum state tomography protocol that relies on the ability to selectively excite each emitter individually by spatially localized pulses. Simulations of coupled semiconductor GaAs/InAs quantum dots using light fields available in current nanoplasmonics show that undesired resonances can be removed from measured spectra. The method can be applied to a broad range of coupled emitters to study the internal coupling, including pigments in photosynthesis and artificial light harvesting.

DOI: [10.1103/PhysRevB.86.085308](https://doi.org/10.1103/PhysRevB.86.085308)

PACS number(s): 78.67.Hc, 03.65.Wj, 78.47.jh, 82.53.Mj

I. INTRODUCTION

The formation of collective optical resonances from Coulomb-coupled optical emitters is a very general phenomenon, including examples from chromophores in biological light harvesting complexes,^{1–4} semiconductor quantum dots,^{5,6} metal nanoparticles, and composite systems, such as plasmon lasers.⁷

For all these structures, dipole-dipole coupling occurs on a nanometer scale and the states of the individual emitters hybridize to form new collective, so-called excitonic states, delocalized over the whole structure. Far-field excitation, governed by the wavelength resolution limit $\lambda/2$, can probe only delocalized exciton states of a nanostructure. Related far-field experiments such as absorption, pump probe, and four-wave mixing are unable to disentangle the individual contributions of the coupled emitters from the collective optical response, because the exciting fields are spatially constant on the scale of the entire structure and cannot discriminate different emitters. In contrast, spatially local spectroscopy such as near-field spectroscopy can, in principle, address the individual emitters.

In this paper, we propose a new class of measurements that combine coherent nonlinear spectroscopy with near-field optics to reconstruct the contributions of single emitters to the delocalized wave function in a spatially extended nanostructure. As an example, we demonstrate how a coherent double-quantum-coherence optical technique⁸ may be combined with spatially localized fields to reconstruct the exciton wave functions of three dipole coupled self-organized GaAs/InAs quantum dots. This constitutes a particular quantum state tomography. The presented procedure is independent of the technique for localizing the fields at individual emitters. Several localization methods are known and are already applied to a broad range of nanoemitting structures, for example, using (metallized) near-field fiber tips,^{5,9,10} metal tips,^{11,12} nano antennas,^{13–17} and metal structures combined with pulse-shaped fields.^{18,19}

Quantum state tomography is a development aimed at the direct reconstruction of wave functions or more generally the density matrix, first proposed by Fano.²⁰ The importance of quantum state tomography results from the fact that the reconstruction and knowledge of the wave function opens the possibility of calculating new observables not related to optics at all. Examples include magnetic moments and transport properties. So far, wave functions are seldom directly accessible by experiments.²¹ Recent advances include imaging of single orbitals using soft x-ray pulses^{22,23} and the reconstruction of states.^{24,25} Applications so far include spin- $\frac{1}{2}$ particles,²⁶ photon states using the Wigner function,^{27,28} vibrational states,²⁹ and Josephson junctions.³⁰ In contrast to earlier approaches, the quantum state tomography developed in this paper combines optical fields, highly localized in time and space with coherent two-dimensional (2D) spectroscopy, using a sequence of light pulses with controlled envelopes and phases.^{8,31,32}

II. EXCITONS IN COUPLED NANOSTRUCTURES

As a typical example for coupled nanostructures with delocalized wave functions, we study three coupled self-organized semiconductor quantum dots^{6,33,34} [Fig. 1(a)]. The quantum-dot distance is assumed to be sufficiently large to have no electronic wave function overlap between the quantum dots. In this case we study interdot coupling in the form of dipole-dipole (or Förster) coupling known from self-organized GaAs/InAs quantum dots: Parameters like dot size, dot distances, coupling constants, and energy shifts are well known from theory³⁵ and experiments.³⁶ Each quantum dot is represented as a two-level system. This is a valid assumption for quantum dots provided quantum dots (i) have no spin-orbit splitting and a sufficiently large biexcitonic shift, (ii) are negatively charged, or (iii) have spin-orbit coupling bigger than the inter-quantum-dot couplings.^{37,38} For self-organized quantum dots with sizes of 20 nm and

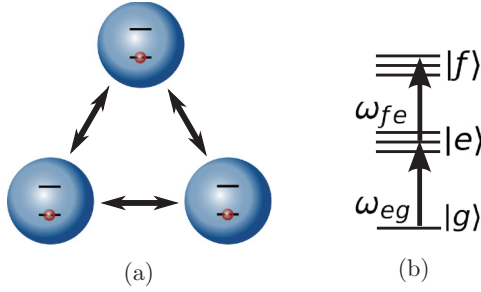


FIG. 1. (Color online) (a) Three dipole-dipole coupled self-organized InAs quantum dots. (b) Exciton level scheme of the three coupled quantum dots.

interdot distances around 40 nm, the dipole coupling is about several μeV with a Lorentzian zero phonon line (ZPL) width of $\gamma = 1 \mu\text{eV}$ at low temperatures (e.g., $T = 4 \text{ K}$).^{38,39} We neglected the influence of the phonon side bands, since their amplitude in the spectra is one to two orders smaller than the amplitude of the ZPL resonance at low temperatures.^{38,39}

Three coupled quantum dots exhibit joint states: a ground state g ; three single-exciton states e_1 , e_2 , and e_3 ; and three two-exciton states f_1 , f_2 , and f_3 [Fig. 1(b)]. The system has one triexciton state, but these states are of no relevance in a third-order optical experiment, considered here. The ground state of the uncoupled quantum dots is not changed by the induced dipole-dipole coupling. The delocalized single-exciton states $|e\rangle$ resulting from the dipole-dipole interaction are composed of local, uncoupled quantum-dot states $|i\rangle$ (quantum dot i in excited state): $|e\rangle = \sum_i c_i^e |i\rangle$. $|e\rangle$ is an energy eigenstate of the coupled quantum-dot system, c_i^e the expansion coefficients. Similarly, two-exciton states $|f\rangle$ are composed of states with two local excitations at quantum dots i and j : $|f\rangle = \sum_{i<j} c_{ij}^f |ij\rangle$. In general, excited states of N coupled two-level system emitters form a ground state g , N delocalized single-exciton states e , and $N(N-1)/2$ delocalized two exciton states f . For our three-dot case, we choose couplings between two quantum dots slightly stronger than to the third quantum dot (parameters given in Table I). Here, H_0 includes along the diagonal the transition-frequency local emitters modified by single- and two-exciton shifts, respectively. The off-diagonal elements describe interactions of excitation transfer caused by, for example, dipole-dipole interactions.

TABLE I. Hamilton operator in matrix form. (a) The single-exciton block and (b) the two-exciton block. All values are given in μeV . The diagonal elements of the matrices are given as detuning to a mean gap frequency, (a) ω_{gap} for the single excitons and (b) $2\omega_{\text{gap}}$ for the two excitons, with $\omega_{\text{gap}} = 1.053 \text{ eV}$ and the two-exciton shifts $V_{11} = 0.1 \mu\text{eV}$, $V_{12} = -2.5 \mu\text{eV}$, and $V_{13} = -1.5 \mu\text{eV}$.

| | $\langle i H_0 j\rangle$ | 1 | 2 | 3 |
|-----|----------------------------|--|--|--|
| (a) | 1 | 2.0 | 1.0 | 0.2 |
| | 2 | 1.0 | 0.2 | 0.1 |
| | 3 | 0.2 | 0.1 | -2.5 |
| (b) | $\langle ij H_0 kl\rangle$ | 1,2 | 1,3 | 2,3 |
| | 1,2 | $\langle 1 H_0 1\rangle + \langle 2 H_0 2\rangle + V_{11}$ | $\langle 3 H_0 2\rangle$ | $\langle 3 H_0 1\rangle$ |
| | 1,3 | $\langle 2 H_0 3\rangle$ | $\langle 1 H_0 1\rangle + \langle 3 H_0 3\rangle + V_{12}$ | $\langle 2 H_0 1\rangle$ |
| | 2,3 | $\langle 1 H_0 3\rangle$ | $\langle 1 H_0 2\rangle$ | $\langle 1 H_0 1\rangle + \langle 3 H_0 3\rangle + V_{13}$ |

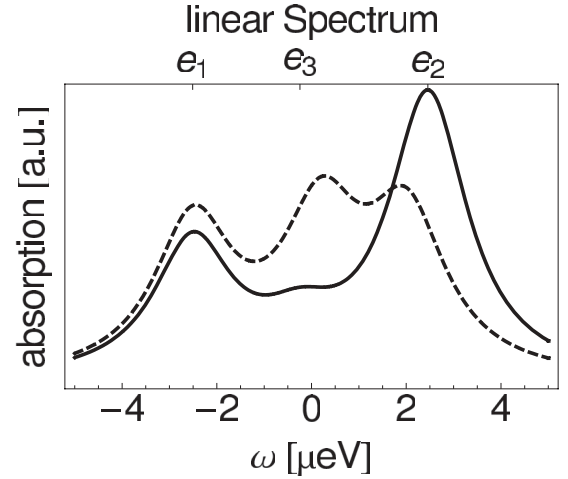


FIG. 2. Absorption spectrum coupled (solid) and uncoupled (dashed) quantum dots. The detection frequency ω is given as detuning relative to frequency $\omega_{\text{gap}} = 1.053 \text{ eV}$ (transition frequency of uncoupled quantum dot 3).

First, to characterize the system within far-field spectroscopy, we calculate the linear absorption spectrum:

$$\alpha(\omega) \propto \sum_e \frac{|\mu_{eg}|^2}{(\omega - \omega_{eg})^2 + \gamma^2}. \quad (1)$$

Here, μ_{eg} is the dipole moment for ground-state to single-exciton transition, ω_{eg} is the transition frequency, and γ is the dephasing constant.

The absorption spectrum of the coupled quantum-dot structure is plotted in Fig. 2 (solid). The single-exciton states e_1 , e_2 , and e_3 overlap spectrally such that only e_1 and e_2 are well resolved and e_3 contributes only with a spectral shoulder. By comparing coupled and uncoupled (dashed) spectra, one recognizes that the oscillator strength is originally evenly distributed but strongly modified, since the dipole-dipole coupling forms excitons delocalized over the entire structure.

III. INGREDIENTS FOR RECONSTRUCTING DELOCALIZED STATES

Our main goal is to gain information on the buildup of the delocalized wave functions of the excitonic states (i.e., on the expansion coefficients c_i^e) for a given single-exciton state $|e\rangle$.

For this purpose, we use coherent, spatially local spectroscopy composed of three ingredients:

(i) local nanoscale excitation provided by metallic nanoantennas and refined pulse-shaping techniques^{19,40} to optically address individual quantum dots (Sec. III A),

(ii) phase cycling of the optical response^{41–43} to disentangle the total nonlinear response into desired quantum paths (Sec. III B), and

(iii) a postprocessing procedure to calculate the coefficients c_i^e (Sec. IV).

In general, (ii) and (iii) can be applied to any quantum system representable by spatially separated coupled emitters, if any localization technique (i) is available.

A. Localized excitation

A main ingredient of our scheme is the local excitation of individual quantum dots. In our specific example, we achieve local excitation of the individual quantum dots by a plasmonic antenna structure of triangular symmetry on a subwavelength scale [Fig. 3(a)]. These metal structures can be realized by e-beam lithography. Solving Maxwell's equations for this geometry shows that plasmonic effects and an optimization procedure of the applied pulses allows us to selectively excite single quantum dots.^{44,45}

For optimizing the pulse envelope of a single pulse $\mathbf{E}(t, \mathbf{r})$ towards a field localization at only one quantum dot, we use time-harmonic solutions $\mathbf{E}_v(\omega, \mathbf{r})$, represented by incident plane waves of polarization directions (superscripts p and s) and incoming direction (indexed as v):⁴⁵

$$\mathbf{E}(t, \mathbf{r}) = \frac{1}{\sqrt{2\pi}} \int_{-\infty}^{\infty} d\omega \sum_v g_v(\omega) \mathbf{E}_v(\omega, \mathbf{r}) e^{-i\omega t}. \quad (2)$$

Pulse shaping is introduced by the weighting function:

$$g_v(\omega) = \sum_n f^v(\vartheta_n) \frac{A_n}{\sqrt{2\pi}} e^{-(\eta_n - \omega)^2 \sigma_n^2 / 2 + i\omega\tau_n + i\beta_n}, \quad (3)$$

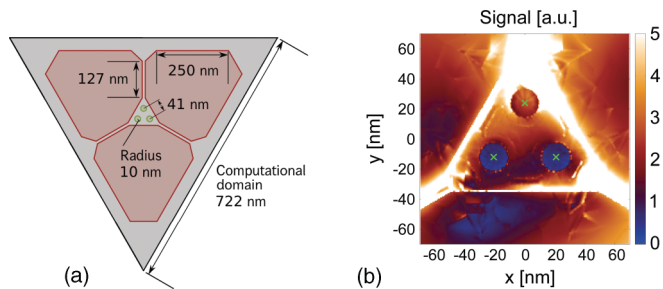


FIG. 3. (Color online) (a) Schematic geometry: Three self-organized GaAs/InAs quantum dots (diameter 20 nm, interdot distances 40 nm) and three 12-nm-thick silver structures, arranged with 120° rotational symmetry on a semi-infinite GaAs layer. (b) Optimized localized electric field $|E|$ at the maximum peak for a single pulse composed from shaped pulses from three different directions. Note: the white color is 5 arbitrary units or higher. The magnitude (extracted at X) of the optimized electric field $|E(\mathbf{r}, \omega_{\text{gap}})|$ for ω_{gap} at dots 2 and 3 is 12% or 7.5% compared to dot 1. The field intensity is scalable while third-order perturbation theory is valid for the double-quantum-coherence spectrum.

which represents a composition of Gaussian pulses with amplitudes A , center times τ , frequencies η , widths σ , phases β , and polarization angle ϑ for each pulse n projected to polarization direction v ($f^p = \cos, f^s = \sin$). $g_v(\omega)$ has to be determined by optimization. To increase the number of optimization parameters, we combine the three incoming pulses from three directions, using 120° symmetry of the sample. For this paper, details of the optimization procedure are of no relevance but can be found in Refs. 40 and 44. Later on, the absolute value of $E(t)$ in the quantum-dot centers is the input for the calculation of the localized spectra.

In Fig. 3(b), the spatial field distribution for the optimized total field around the quantum-dot transition frequency is shown. It can be recognized that a chosen, single quantum dot is excited stronger than the other quantum dots. We observe field enhancements between different quantum dot sites of a factor of eight or larger. Note that the optimized fields in frequency domain show that polarization and propagation phase effects cause localization and not a frequency-based selection of different quantum dots.

Note that the presented localization scheme using excitation pads is just an example. For application of the protocol to other systems,^{5,9–19} other spatial localization schemes might be used.

B. Phase cycling detection of coherent signals

As explained in Sec. III A, a sequence of three spatially optimized pulse envelopes E^i with phases φ_i and laser frequency ω_l is used:^{8,46}

$$\begin{aligned} E(\mathbf{r}, t) = & E^1(\mathbf{r}, t - t_3 - t_2 - t_1) e^{i\omega_l(t - t_3 - t_2 - t_1) + i\varphi_1} \\ & + E^2(\mathbf{r}, t - t_3 - t_2) e^{i\omega_l(t - t_3 - t_2) + i\varphi_2} \\ & + E^3(\mathbf{r}, t - t_3) e^{i\omega_l(t - t_3) + i\varphi_3} + \text{c.c.} \end{aligned} \quad (4)$$

Here the envelopes $E^i(\mathbf{r}, t)$ are determined by the optimization procedure for localized pulses. The detected signal (selected quantum pathways of the full dipole density) is measured with heterodyne detection via phase cycling^{41–43,47} by repeating the experiment several times for different phases φ_1, φ_2 , and φ_3 [Fig. 4(a)].

In general the polarization, created by three pulses applied to the quantum dots, is described by many quantum pathways in Liouville space.⁸ In the following way, we can extract a subset of the Liouville pathways by extracting a certain phase combination of φ_1, φ_2 , and φ_3 . The detected dipole density for different phases can be written as⁴¹

$$\begin{aligned} P(t, \varphi_1, \varphi_2, \varphi_3) = & \mathcal{P}(t, \varphi_1, \varphi_2, \varphi_3) + \text{c.c.}, \\ \mathcal{P}(t, \varphi_1, \varphi_2, \varphi_3) = & \sum_{lmn} c_{123,lmn} P_{lmn}(t), \end{aligned} \quad (5)$$

with $c_{123,lmn} = e^{i(l\varphi_1 + m\varphi_2 + n\varphi_3)}$, $l + m + n = 1$, and $|l| + |m| + |n| = 1$ or 3 for resonant excitation and $P_{lmn}(t)$ being the part of the detected polarization with phase dependence $l\varphi_1 + m\varphi_2 + n\varphi_3$. $c_{123,lmn}$ can be viewed as a matrix with first index $(\varphi_1, \varphi_2, \varphi_3)$ and second index (l, m, n) . By carrying out the experiment for sufficient phase combinations $\varphi_1, \varphi_2, \varphi_3$, so that the matrix $c_{123,lmn}$ is invertable, we can extract the signal with a specific phase combination $\varphi_4 = l\varphi_1 + m\varphi_2 + n\varphi_3$ (selecting particular pathways) using $P_{lmn}(t) = \sum_{1,2,3} c_{123,lmn}^{-1} \mathcal{P}(t, \varphi_1, \varphi_2, \varphi_3)$. Details of this phase-cycling

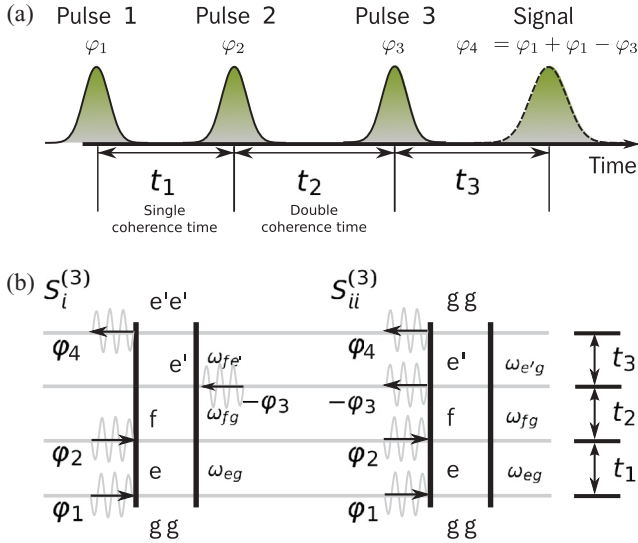


FIG. 4. (Color online) (a) Pulse sequence for the double-quantum-coherence experiment. (b) The two density matrix pathways S_i and S_{ii} [Eq. (20)]. See text for more details.

procedure can be found in Ref. 41. Typical examples for such signals are the photon echo $\varphi_4 = -\varphi_1 + \varphi_2 + \varphi_3$ and antiphoton echo $\varphi_4 = \varphi_1 - \varphi_2 + \varphi_3$ (cf. Ref. 8).

C. Double-quantum-coherence signal

We focus on the double-quantum-coherence signal, a third-order signal with the contributing phase combinations $\varphi_4 = \varphi_1 + \varphi_2 - \varphi_3$.^{8,46} In the case of a system where the ground state, single-exciton state, and two-exciton state form three bands [Fig. 1(b)], only the two Liouville pathways depicted in Fig. 4(b) will contribute to the signal with $\varphi_4 = \varphi_1 + \varphi_2 - \varphi_3$.^{8,46}

In the case of the three-band model [Fig. 1(b)] only two Liouville pathways can contribute. The part of the polarization attributed to φ_4 , i.e., $P_{1,1-1}^{(3)}(t)$, which depends on the delay times can be written using a response function:⁸

$$P_{1,1-1}^{(3)}(t) = \int_0^\infty d\tau_3 \int_0^\infty d\tau_2 \int_0^\infty d\tau_1 \times R_{1,1-1}^{(3)}(t, t - \tau_3, t - \tau_3 - \tau_2, t - \tau_3 - \tau_2 - \tau_1). \quad (6)$$

Note that we include the optical fields in the definition of the response, which is rather uncommon, but for the use of localized fields this notation will simplify the discussion. The response function $R_{1,1-1}^{(3)}$ can be divided into the contributions of two Liouville pathways, extracted from the full response function.⁸

$$R^{(3)}(t, \tilde{t}_3, \tilde{t}_2, \tilde{t}_1) = \left(\frac{t}{\hbar}\right)^3 \text{tr}[\mu \mathcal{G}(t - \tilde{t}_3) H_{el-L,-}(\tilde{t}_3) \mathcal{G}(\tilde{t}_3 - \tilde{t}_2) \times H_{el-L,-}(\tilde{t}_2) \mathcal{G}(\tilde{t}_2 - \tilde{t}_1) H_{el-L,-}(\tilde{t}_1) \rho_0]. \quad (7)$$

Here, the electron electric-field interaction Liouvillian $H_{el-L,-}(t)\rho = [H_{el-L}(t), \rho]$, Green's function $\mathcal{G}(t)$ with $\mathcal{G}(t)\rho(t) = \theta(t)\exp(-\frac{i}{\hbar}H_0t)\rho(t)\exp(\frac{i}{\hbar}H_0t)$, and the dipole operator $\mu = \sum_i \mu_{gi}|g\rangle\langle i| + \text{h.a.}$ For our excitonic three-band

system, for the far-field excitation we insert the light-matter Hamiltonian in local basis:

$$H_{el-L} = \sum_i \mu_{gi} \cdot E(t)|g\rangle\langle i| + \sum_{ij} \mu_{gi} \cdot E(t)|j\rangle\langle ij| + \text{H.a.} \quad (8)$$

The Hamilton operator can also be reformulated in the delocalized basis:

$$H_{el-L} = \sum_e \mu_{ge} \cdot E(t)|g\rangle\langle e| + \sum_{ef} \mu_{ef} \cdot E(t)|e\rangle\langle f| + \text{H.a.}, \quad (9)$$

with the delocalized exciton dipole matrix elements $\mu_{ge} = \sum_i c_i^e \mu_{gi}$ and $\mu_{ef} = \sum_{i<j} c_i^{e*} \mu_{gi} c_j^f$. We insert Eq. (9) into Eq. (7) and collect for $R_{1,1-1}^{(3)}$ only the terms proportional to $\exp[i(-\varphi_3 + \varphi_2 + \varphi_1)]$ and end up with the response from two contributing Liouville pathways [Fig. 4(b)] assuming no temporal pulse overlap:⁸

$$R_{1,1-1}^{(3)}(t, \tilde{t}_3, \tilde{t}_2, \tilde{t}_1) = R_i^{(3)}(t, \tilde{t}_3, \tilde{t}_2, \tilde{t}_1) + R_{ii}^{(3)}(t, \tilde{t}_3, \tilde{t}_2, \tilde{t}_1), \quad (10)$$

$$R_i^{(3)}(t, \tilde{t}_3, \tilde{t}_2, \tilde{t}_1) = -\left(\frac{t}{\hbar}\right)^3 e^{i\omega_l(\tilde{t}_1 + \tilde{t}_2 - \tilde{t}_3 - t_1 - 2t_2 - t_3)} \times \sum_{e'e'f} \mu_{e'f} \mu_{ge'} \cdot E^{3*}(\tilde{t}_3 - t_3) \times \mu_{fe} \cdot E^2(\tilde{t}_2 - t_3 - t_2) \times \mu_{eg} \cdot E^1(\tilde{t}_1 - t_3 - t_2 - t_1) \times e^{-i\xi_{f'e'}(t - \tilde{t}_3) - i\xi_{fg}(\tilde{t}_3 - \tilde{t}_2) - i\xi_{eg}(\tilde{t}_2 - \tilde{t}_1)}, \quad (11)$$

$$R_{ii}^{(3)}(t, \tilde{t}_3, \tilde{t}_2, \tilde{t}_1) = \left(\frac{t}{\hbar}\right)^3 e^{i\omega_l(\tilde{t}_1 + \tilde{t}_2 - \tilde{t}_3 - t_1 - 2t_2 - t_3)} \times \sum_{e'e'f} \mu_{ge'} \mu_{e'f} \cdot E^{3*}(\tilde{t}_3 - t_3) \times \mu_{fe} \cdot E^2(\tilde{t}_2 - t_3 - t_2) \times \mu_{eg} \cdot E^1(\tilde{t}_1 - t_3 - t_2 - t_1) \times e^{-i\xi_{e'g}(t - \tilde{t}_3) - i\xi_{fg}(\tilde{t}_3 - \tilde{t}_2) - i\xi_{eg}(\tilde{t}_2 - \tilde{t}_1)}. \quad (12)$$

Here, $\xi_{nm} = \omega_{nm} - i\gamma_{nm}$, with $\omega_{nm} = \omega_n - \omega_m$ including the exciton frequencies ω_n and the dephasing and relaxation rate γ_{nm} for a Lorentzian dephasing model.

In both pathways i and ii, we have a coherence between the single-exciton and ground states in between the first and second pulses and a coherence between the two-exciton to ground states in between the second and third pulses. After the third pulse the system is either in a single-exciton to two-exciton coherence (pathway i) or ground-state to single-exciton coherence (pathway ii). We consider for further analysis the heterodyne detected signal, where the emitted signal $P_{1,1-1}^{(3)}(t)$ is mixed with the field of a local oscillator E_4 :

$$S_{k_{III}}^{(3)}(t_1, t_2, t_2) = \int_{-\infty}^{\infty} dt P_{1,1-1}^{(3)}(t) \cdot E^{4*}(t) e^{i\omega_l t}. \quad (13)$$

$S_{k_{III}}^{(3)}(t_1, t_2, t_2)$ is a complex quantity. A measurement obtains the real part of $S_{k_{III}}^{(3)}(t_1, t_2, t_2)$.⁸ However, the use of a local oscillator in heterodyne detection allows—by twisting its

phase—to detect the imaginary part of the signal^{2,8,31,48–50} (phase-cycled detection of fluorescence in the fourth order³² can give similar information as heterodyne-detected signals in third order); this works both for the signal in temporal and Fourier domain. It is therefore a preferred method to extract also the phase information of the coefficients c_i^e ; most other methods will only extract the absolute value.

In order to separate the different coherences of the signal by their energies, the signal is Fourier transformed over the delay times:⁸

$$S_{k_{III}}^{(3)}(\Omega_1, \Omega_2, t_3) = \int_0^\infty dt_1 \int_0^\infty dt_2 e^{i\Omega_1 t_1 + i\Omega_2 t_2} S_{k_{III}}^{(3)}(t_1, t_2, t_3). \quad (14)$$

For the analysis, the double-quantum-coherence signal $S_{k_{III}}^{(3)}$ is plotted as a function of the frequencies Ω_1, Ω_2 [Fig. 4(a)]:

$$S_{k_{III}}^{(3)}(\Omega_1, \Omega_2, t_3) = S_i^{(3)}(\Omega_1, \Omega_2, t_3) + S_{ii}^{(3)}(\Omega_1, \Omega_2, t_3), \quad (15)$$

$$\begin{aligned} S_i^{(3)}(\Omega_1, \Omega_2, t_3) &= \frac{1}{\hbar^3} \sum_{e'f} \mu_{e'f} \cdot E^{4*}(\omega_{f'e'}) \mu_{g'e'} \cdot E^{3*}(\omega_{e'g}) \\ &\times \mu_{ef}^* \cdot E^2(\omega_{fe}) \mu_{ge}^* \cdot E^1(\omega_{eg}) \frac{\exp(-i\xi_{f'e'} t_3)}{(\Omega_2 - \xi_{fg})(\Omega_1 - \xi_{eg})}, \end{aligned} \quad (16)$$

$$\begin{aligned} S_{ii}^{(3)}(\Omega_1, \Omega_2, t_3) &= -\frac{1}{\hbar^3} \sum_{e'f} \mu_{g'e'} \cdot E^{4*}(\omega_{e'g}) \mu_{e'f} \cdot E^{3*}(\omega_{f'e'}) \\ &\times \mu_{ef}^* \cdot E^2(\omega_{fe}) \mu_{ge}^* \cdot E^1(\omega_{eg}) \frac{\exp(-i\xi_{e'g} t_3)}{(\Omega_2 - \xi_{fg})(\Omega_1 - \xi_{eg})}. \end{aligned} \quad (17)$$

It exhibits resonances for the ground-state–single-exciton transitions ω_{eg} along the Ω_1 axis and the ground-state–two-exciton transition ω_{fg} ^{8,46} along the Ω_2 axis. Due to the use of the local oscillator, the imaginary and real parts of $S_{k_{III}}^{(3)}(\Omega_1, \Omega_2, t_3)$ can be obtained from experimental data.⁸

D. Localized double-quantum-coherence signal

For the localized spectroscopy described here, the double-quantum-coherence signal $S_{k_{III}}^{(3)}$ ^{8,46} is modified by localizing the first pulse at a specific quantum dot i [Fig. 3(b)]. For a localized excitation, the Hamiltonian Eq. (8) must be modified:

$$\begin{aligned} H_{el-L} &= \sum_i \mu_{gi} \cdot E(r_i, t) |g\rangle \langle i|_l \\ &+ \sum_{ij} \mu_{gi} \cdot E(r_i, t) |j\rangle \langle ij|_l + \text{H.a.} \end{aligned} \quad (18)$$

and yields

$$\begin{aligned} H_{el-L} &= \sum_{ie} c_i^e \mu_{gi} \cdot E(r_i, t) |g\rangle \langle e| \\ &+ \sum_{i < jef} c_i^{e*} \mu_{gi} c_{ij}^f \cdot E(r_i, t) |e\rangle \langle f| + \text{H.a.} \end{aligned} \quad (19)$$

for the delocalized states. We see that no delocalized dipole moments are formed, since the effective response depends on the spatial distribution of the electric field.

Using far-field excitation for pulses E^2 and E^3 , the local oscillator E^4 for heterodyne detection, and a localized excitation for the first pulse E^1 at dot i ($E^1 \rightarrow E_i^1$), the double-quantum-coherence signal $S_{k_{III}}^{(3)}(i, \Omega_1, \Omega_2, t_3) = S_i^{(3)}(i, \Omega_1, \Omega_2, t_3) + S_{ii}^{(3)}(i, \Omega_1, \Omega_2, t_3)$ now depends on the chosen quantum dot i and reads

$$S_{k_{III}}^{(3)}(i, \Omega_1, \Omega_2, t_3) = S_i^{(3)}(i, \Omega_1, \Omega_2, t_3) + S_{ii}^{(3)}(i, \Omega_1, \Omega_2, t_3) \quad (20)$$

$$\begin{aligned} S_i^{(3)}(i, \Omega_1, \Omega_2, t_3) &= \frac{1}{\hbar^3} \sum_{e'fj} \mu_{e'f} \cdot E^{4*}(\omega_{f'e'}) \mu_{g'e'} \cdot E^{3*}(\omega_{e'g}) \\ &\times \mu_{ef}^* \cdot E^2(\omega_{fe}) c_j^{e*} \mu_{gj}^* \cdot E_i^1(\mathbf{r}_j, \omega_{eg}) \\ &\times \frac{\exp(-i\xi_{f'e'} t_3)}{(\Omega_2 - \xi_{fg})(\Omega_1 - \xi_{eg})}, \end{aligned} \quad (21)$$

$$\begin{aligned} S_{ii}^{(3)}(i, \Omega_1, \Omega_2, t_3) &= -\frac{1}{\hbar^3} \sum_{e'fj} \mu_{g'e'} \cdot E^{4*}(\omega_{e'g}) \mu_{e'f} \cdot E^{3*}(\omega_{f'e'}) \\ &\times \mu_{ef}^* \cdot E^2(\omega_{fe}) c_j^{e*} \mu_{gj}^* \cdot E_i^1(\mathbf{r}_j, \omega_{eg}) \\ &\times \frac{\exp(-i\xi_{e'g} t_3)}{(\Omega_2 - \xi_{fg})(\Omega_1 - \xi_{eg})}. \end{aligned} \quad (22)$$

μ_{eg} (μ_{fe}) are single-exciton (two-exciton) to ground state (single-exciton) dipoles in the delocalized basis, and μ_{gi} is the dipole moment for the ground-state to excited-state transition of quantum dot i . $E_i^1(\mathbf{r}_j, \omega_{eg})$ is the first pulse, predominantly exciting quantum dot i , only weakly exciting the other quantum dots with $i \neq j$. We assume ideal localization by taking $E_i^1(\mathbf{r}_j, \omega_{eg}) \approx \delta_{ij} E_i^1(\mathbf{r}_i, \omega_{eg})$.

E. Discussion of the double-quantum-coherence signal

Figure 5 shows the far-field double-quantum-coherence signal [$E_i^1(\mathbf{r}_j, \omega) \approx E^1(\omega)$, cf. Sec. III C] absolute value [Fig. 4(a)] and imaginary value [Fig. 4(b)]: The frequency of the single-exciton to ground-state coherence can be seen on the Ω_1 axis and the frequency of the two-exciton to ground-state coherence on the Ω_2 axis. Clearly, for the far-field excitation in Figs. 5(a) and 5(b) we see resonances connecting to coherence of several states e and f . If we select a frequency $\Omega_1 = \omega_{e,g}$, we see along the Ω_2 axis which specific two-exciton states are connected via dipole moments to the single-exciton state e_i and vice versa. A comparison of the dipole moments connected to two different peaks works only roughly, since two Liouville paths interfere and the degree of destructive interference is different for every peak.

A dominant peak (A) in the absolute value spectrum [Fig. 5(a)] is connected to e_2 and f_2 , a second strong peak is connected to e_2 and f_1 , and some further peaks with smaller oscillator strength can be seen at a lower single-exciton energy (e_3 and f_2, e_1 and f_1). e_1 and e_2 are well resolved, and e_3 shows up as a spectral shoulder. This shows that the system has three single-exciton and three two-exciton states.

Figure 5(c) shows the signal with the first pulse localized at either quantum dots 1, 2, or 3. The localization of the first pulse

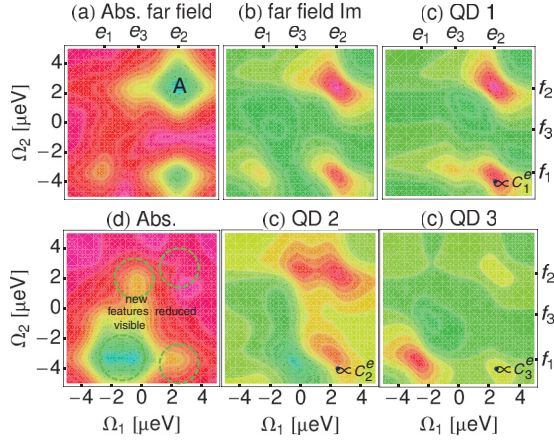


FIG. 5. (Color online) DQS for $t_3 = 200$ ps (a) absolute value and (b) imaginary part, Ω_1 (Ω_2) given as detuning around the single (double) gap frequency ω_{gap} . (c) Imaginary part of localized double-quantum-coherence spectrum, where the first pulse is localized at quantum dots 1, 2, and 3 as indicated. (d) Filtered standard double-quantum-coherence spectrum (e_2 removed).

gives information about the single-exciton states contributing to the ground-state–single-exciton transition occurring during the first pulse. Localization at quantum dot (QD) 1 shows that all resonances connected to the delocalized exciton state e_1 disappear. Overall, this shows that quantum dot 1 contributes strongly only to the formation of single-exciton states e_2 and e_3 but not to the buildup of e_1 . Similar information is obtained for excitation of quantum dots 2 and 3 [see Fig. 5(c)]. For example, the exciton state e_2 is formed by quantum dots 1 and 2. Another interesting feature is the peak connecting e_3 and f_1 . This peak is only visible at the localized spectrum at QD 2 and QD 3 and not in the far-field spectrum. This is caused by the fact that e_3 is an antisymmetric delocalized state between QDs 2 and 3, seen by the opposite sign of the peak in the QD 2 and QD 3 spectrum. For far-field excitation, these two antiparallel dipoles interfere destructively, so that the resonance is not observed.

We next use the localized double quantum coherence to extract the wave function coefficients c_i^e and therefore all quantum dot interactions.

IV. EXTRACTING THE SINGLE-EXCITON WAVE FUNCTION

All ingredients are now available to extract the single-exciton wave function. We start from the localized signal in Eqs. (20)–(22) and see that the sum over e and j prevents us from extracting a particular coefficient c_i^e . Assuming ideal localization of the first pulse at a particular quantum dot i [$E_i^1(\mathbf{r}_j, \omega_{eg}) \approx \delta_{ij} E_i^1(\mathbf{r}_i, \omega_{eg})$] removes the sum over j in Eqs. (20)–(22). Of course, any deviation from ideal localization will result in an error in the measurement of the coefficients (see below).

For removing the sum over e and selecting a particular single-exciton state e , we choose the frequencies $\Omega_1 = \Omega_1^e$ and $\Omega_2 = \Omega_2^e$ in a way that only a specific peak caused by single-exciton to ground state ω_{eg} and two-exciton to

ground state coherences ω_{fg} connected to e contributes, as suggested by the denominators in Eqs. (20)–(22). Again, if peaks for different single-exciton states overlap, errors are introduced to the reconstruction. (However, two-dimensional spectroscopy has less spectral overlap than one-dimensional spectroscopy, since the peaks are separated by an additional degree of freedom: the additional frequency axis.) This yields

$$S_{k_{III}}^{(3)}(i, \Omega_1^e, \Omega_2^e, t_3) = S_i^{(3)}(i, \Omega_1^e, \Omega_2^e, t_3) + S_{ii}^{(3)}(i, \Omega_1^e, \Omega_2^e, t_3), \quad (23)$$

$$S_i^{(3)}(i, \Omega_1^e, \Omega_2^e, t_3) \approx \frac{1}{\hbar^3} \sum_{e'f} \mu_{e'f} \cdot E^{4*}(\omega_{f'e'}) \mu_{g'e'} \cdot E^{3*}(\omega_{e'g}) \times \mu_{ef}^* \cdot E^2(\omega_{fe}) c_i^{e*} \mu_{gi}^* \cdot E_i^1(\mathbf{r}_i, \omega_{eg}) \times \frac{\exp(-t \xi_{f'e'} t_3)}{(\Omega_2 - \xi_{f'e'}) (\Omega_1 - \xi_{eg})}, \quad (24)$$

$$S_{ii}^{(3)}(i, \Omega_1, \Omega_2, t_3) \approx -\frac{1}{\hbar^3} \sum_{e'f} \mu_{g'e'} \cdot E^{4*}(\omega_{e'g}) \mu_{e'f} \cdot E^{3*}(\omega_{f'e'}) \times \mu_{ef}^* \cdot E^2(\omega_{fe}) c_i^{e*} \mu_{gi}^* \cdot E_i^1(\mathbf{r}_i, \omega_{eg}) \times \frac{\exp(-t \xi_{e'g} t_3)}{(\Omega_2 - \xi_{f'e'}) (\Omega_1 - \xi_{eg})}. \quad (25)$$

We see that here the double-quantum-coherence signal is proportional to $c_i^{e*} \mu_{gi}^* \cdot E_i^1(\mathbf{r}_i, \omega_{eg})$, that is, to the strength c_i^{e*} the i th quantum dot contributes to the delocalized wave function. This fact is used to develop a scheme to extract the coefficients c_i^e from measured data:

As **input information**, the dipole moments μ_{gi} of the individual uncoupled quantum dots are required, and the dipole moments can be measured or calculated. As **measurement**, carry out the localized double-quantum-coherence signal $S_{k_{III}}^{(3)}(i, \Omega_1, \Omega_2, t_3)$, for a localization on all quantum dots i . If the field strength and polarization direction are different for localization at different quantum dots, we need to obtain the electric field along the local dipole $\mu_{gi}^* \cdot E_i^1(\mathbf{r}_i, \omega_{eg})$.

Now, we select the excitonic state $e \equiv e_\alpha$, whose coefficients $c_i^{e_\alpha}$ should be extracted. We determine the frequencies $\Omega_1 \approx \omega_{e_\alpha g}$, $\Omega_2 \approx \omega_{f_\beta g}$ showing a strong correlation to e_α using the double-quantum-coherence signal without spatial localization. Now in the **postprocessing** of the data, we use that $c_i^{e_\alpha} \propto S_{k_{III}}^{(3)} / [\mu_{gi}^* \cdot E_i^1(\mathbf{r}_i, \omega_{eg})]$ at the positions $\Omega_1 \approx \omega_{e_\alpha g}$, $\Omega_2 \approx \omega_{f_\beta g}$ [Eqs. (23)–(25)]. $c_i^{e_\alpha}$ can now be determined up to an proportionality factor A : $c_i^{e_\alpha} A = S_{k_{III}}^{(3)} / [\mu_{gi}^* \cdot E_i^1(\mathbf{r}_i, \omega_{eg})]$ for every quantum dot i , using the same frequencies Ω_1, Ω_2 . Since the wave function is normalized, $|A|^2 = \sum_i |A c_i^{e_\alpha}|^2$ holds. We thus get A up to a global phase and set $A = |A|$. We obtain $c_i^{e_\alpha} = S_{k_{III}}^{(3)}(i, \Omega_1, \Omega_2, t_3) / [\mu_{gi}^* \cdot E_i^1(\mathbf{r}_i, \omega_{eg}) A]$. This gives the delocalized wave function $|e_\alpha\rangle = \sum_i c_i^{e_\alpha} |i\rangle$.

Note that these steps constitutes a quantum state tomography. The local basis is uniquely determined up to an arbitrary phase for every quantum dot: The expansion coefficient c_i^e depends on that choice.

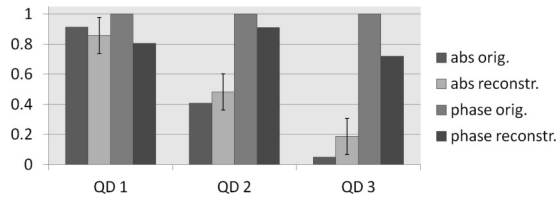


FIG. 6. Original and reconstructed coefficients of single-exciton wave function e_2 : Phase in multiples of 2π . Error of absolute values determined by localization.

To demonstrate the success of the tomography, we compare in Fig. 6 the elements of the reconstructed wave function for the strongest contribution, that is, state e_2 [marked with A in Fig. 5(a)], to the original wave function resulting from the input parameters in the Hamiltonian. The agreement for both the amplitude and the relative phase is quite good. The difference results from a nonperfect localization $E_i^1(\mathbf{r}_j, \omega_{eg}) \neq \delta_{ij} E_i^1(\mathbf{r}_i, \omega_{eg})$ resulting from realistic Maxwell simulation from Sec. III A. This error is marked by the error bars in Fig. 6. It is caused by a weak excitation of quantum dots, which an ideally localized pulse should not excite. Such a nonideal excitation leads to cross talk between the coefficients. The error bars are estimated to be smaller than $\Delta_{e_i} = \sum_{j \neq i} |E_i(\mathbf{r}_j)| / |E_i(\mathbf{r}_i)|$.

Note that in general the procedure works also for other methods than heterodyne detection in the far field, including a localized detection of polarization or fluorescence, as long as the detection is the same for a localization of the first pulse at different quantum dots. The only limitation is that the phase of the coefficients can be detected only with methods that can measure complex signals. For other types of detection, like homodyne detection, we can also extract the absolute value of the coefficients but not their phase.

V. FILTERING COHERENT SPECTRA

As additional useful application, we show that strong, undesired resonances can be selectively suppressed from coherent spectra. This can be advantageous while investigating weak resonances that are masked by other strong resonances: Often, it is not clear whether weak resonances constitute a vibrational side peak connected to a dominating strong excitonic peak or a different, much weaker excitonic resonance. This can also be solved by selectively removing excitonic resonances from measured spectra and applying a filter algorithm.

As **input information** for the filter algorithm, we have to determine expansion coefficients $c_i^{e_\alpha}$ for the specific state e_α for all quantum dots i whose contributions we want to filter out. Additionally, we need all dipole moments μ_{gi} of the individual nanostructure and also the electric field along the local dipole $\mu_{gi}^* \cdot E_i^1(\mathbf{r}_i, \omega_{eg})$.

As **measurement** we record a localized version of the spectrum to be filtered. The localized pulse should excite a ground-state to single-exciton transition for all quantum-dot positions. For the double quantum coherence, this will be the signal $S_{k_{III}}(i, \Omega_1, \Omega_2, t_3)$ for every quantum dot i .

For **postprocessing** we discuss the expression

$$\begin{aligned} S_{k_{III}, w/o e_\alpha}(\Omega_1, \Omega_2, t_3) &= S_{k_{III}}(\Omega_1, \Omega_2, t_3) - \sum_i c_i^{e_\alpha} \mu_{ig}^* \cdot E^1(\omega_{eg}) f_{e_\alpha}(\Omega_1, \Omega_2, t_3) \\ &= \sum_{e' \neq e_\alpha, i} c_i^{e'} \mu_{ig}^* \cdot E_i^1(\omega_{eg}) f_{e'}(\Omega_1, \Omega_2, t_3), \quad (26) \\ f_{e_\alpha}(\Omega_1, \Omega_2, t_3) &= \sum_i c_i^{e_\alpha} S_{k_{III}}(i, \Omega_1, \Omega_2, t_3) / [\mu_{ig}^* \cdot E_i^1(\mathbf{r}_i, \omega_{eg})], \quad (27) \end{aligned}$$

which gives a spectrum where all contribution of e_α during the first pulse are filtered out.⁵¹

The single-exciton peak e_2 ($\alpha = 2$) dominating the spectrum in Fig. 5(a) is filtered out in Fig. 5(d). This spectrum reveals information about states initially covered by the dominant contribution of e_2 . The procedure can be applied iteratively, using the filtered spectra for obtaining the other excitonic states. This can enhance the reconstruction of the exciton states.

The filtering method can also be applied to other spectroscopic signals as long as a phase-sensible detection is used and a localized signal, whose contributions are proportional to the single-exciton expansion coefficients, can be measured.

VI. CONCLUSION AND OUTLOOK

The presented quantum state tomography for the extraction of the delocalized single-exciton wave function coefficients can also be applied to other impulsive two-dimensional spectra. The single-exciton to two-exciton transition in double quantum coherence using the localization of the second pulse also can be used to extract the two exciton coefficients. However, since this problem is more complex, it will be the subject of future work.

In conclusion, our simulations demonstrate a quantum state tomography that can be used to reconstruct individual wave functions of coupled emitters acting only collectively in the far field. In addition, localized excitations are useful to remove unwanted strong resonances to uncover weak or hidden excitonic resonances. All of these features are not accessible in standard far-field spectroscopy. Similar configurations can be alternatively achieved by applying four pulses and using phase cycling to detect a desired component,⁴³ for example, with phase $\varphi = \varphi_1 + \varphi_2 - \varphi_3 - \varphi_4$. We therefore believe that the proposed quantum state tomography opens a new path for the detection of many-body interactions on the nanoscale. The proposed protocol is more general as presented here, since fluorescence can also be used rather than heterodyne detection of optical fields.⁴³

ACKNOWLEDGMENTS

We gratefully acknowledge support from the Deutsche Forschungsgemeinschaft (DFG) through SPP 1391 (M.R., Fe.S., Fr.S.), GRK 1558 (M.S.), and SFB 951 (A.K.). M.R. also acknowledges support from the Alexander von Humboldt Foundation through the Feodor-Lynen program. S.M. gratefully acknowledges the support of NSF Grant CHE-1058791,

DARPA BAA-10-40 QUBE, and the Chemical Sciences, Geosciences, and Biosciences Division, Office of Basic Energy Sciences, Office of Science, US Department of Energy. We

also thank Jens Förstner and Torsten Meier Paderborn for very valuable discussions about the application of the genetic algorithm for the localized fields.

*marten.richter@tu-berlin.de

- ¹G. S. Engel, T. R. Calhoun, E. L. Read, T.-K. Ahn, T. Mancal, Y.-C. Cheng, R. E. Blankenship, and G. R. Fleming, *Nature (London)* **446**, 782 (2007).
- ²N. Christensson, F. Milota, A. Nemeth, I. Pugliesi, E. Riedle, J. Sperling, T. Pullerits, H. F. Kauffmann, and J. Hauer, *J. Phys. Chem. Lett.* **1**, 3366 (2010).
- ³A. D. Wit, ed., *22nd Solvay Conference on Chemistry*, Procedia Chemistry Vol. 3 (Elsevier, Amsterdam, 2011), pp. 1–366.
- ⁴M. Schoth, M. Richter, A. Knorr, and T. Renger, *Phys. Rev. Lett.* **108**, 178104 (2012).
- ⁵T. Guenther, C. Lienau, T. Elsaesser, M. Glanemann, V. M. Axt, T. Kuhn, S. Eshlaghi, and A. D. Wieck, *Phys. Rev. Lett.* **89**, 057401 (2002).
- ⁶B. W. Lovett, J. H. Reina, A. Nazir, and G. A. D. Briggs, *Phys. Rev. B* **68**, 205319 (2003).
- ⁷D. J. Bergman and M. I. Stockman, *Phys. Rev. Lett.* **90**, 027402 (2003).
- ⁸D. Abramavicius, B. Palmieri, D. V. Voronine, F. Sanda, and S. Mukamel, *Chem. Rev.* **109**, 2350 (2009).
- ⁹G. von Freymann, T. Schimmel, M. Wegener, B. Hanewinkel, A. Knorr, and S. W. Koch, *Appl. Phys. Lett.* **73**, 1170 (1998).
- ¹⁰T. Guenther, V. Emiliani, F. Intonti, C. Lienau, T. Elsaesser, R. Notzel, and K. H. Ploog, *Appl. Phys. Lett.* **75**, 3500 (1999).
- ¹¹B. Pettinger, B. Ren, G. Picardi, R. Schuster, and G. Ertl, *Phys. Rev. Lett.* **92**, 096101 (2004).
- ¹²A. Weber-Bargioni, A. Schwartzberg, M. Cornaglia, A. Ismach, J. J. Urban, Y. Pang, R. Gordon, J. Bokor, M. B. Salmeron, D. F. Ogletree, P. Ashby, and S. A. Cabrini, *Nano Lett.* **11**, 1201 (2011).
- ¹³Z. Zhang, A. Weber-Bargioni, S. W. Wu, S. Dhuey, S. Cabrini, and P. J. Schuck, *Nano Lett.* **9**, 4505 (2009).
- ¹⁴A. Kinkhabwala, Z. Yu, S. Fan, Y. Avlasevich, K. Mullen, and W. E. Moerner, *Nat. Photon.* **3**, 654 (2009).
- ¹⁵J. A. Schuller, E. S. Barnard, W. Cai, Y. C. Jun, J. S. White, and M. L. Brongersma, *Nat. Mat.* **9**, 193 (2010).
- ¹⁶A. G. Curto, G. Volpe, T. H. Taminiau, M. P. Kreuzer, R. Quidant, and N. F. van Hulst, *Science* **329**, 930 (2010).
- ¹⁷L. Novotny, *Phys. Today* **64**, 47 (2011).
- ¹⁸M. I. Stockman, S. V. Faleev, and D. J. Bergman, *Phys. Rev. Lett.* **88**, 067402 (2002).
- ¹⁹M. Aeschlimann, M. Bauer, D. Bayer, T. Brixner, F. J. G. de Abajo, W. Pfeiffer, M. Rohmer, C. Spindler, and F. Steeb, *Nature (London)* **446**, 301 (2007).
- ²⁰U. Fano, *Rev. Mod. Phys.* **29**, 74 (1957).
- ²¹I. Gerhardt, G. Wrigge, J. Hwang, G. Zumofen, and V. Sandoghdar, *Phys. Rev. A* **82**, 063823 (2010).
- ²²H. Kapteyn, O. Cohen, I. Christov, and M. Murnane, *Science* **317**, 775 (2007).
- ²³P. B. Corkum and F. Krausz, *Nat. Phys.* **3**, 381 (2007).
- ²⁴J. Yuen-Zhou and A. Aspuru-Guzik, *J. Chem. Phys.* **134**, 134505 (2011).
- ²⁵M. Lobino, D. Korystov, C. Kupchak, E. Figueroa, B. C. Sanders, and A. I. Lvovsky, *Science* **322**, 563 (2008).
- ²⁶W. Band and J. L. Park, *Am. J. Phys.* **47**, 188 (1979).
- ²⁷K. Vogel and H. Risken, *Phys. Rev. A* **40**, 2847 (1989).
- ²⁸D. T. Smithey, M. Beck, M. G. Raymer, and A. Faridani, *Phys. Rev. Lett.* **70**, 1244 (1993).
- ²⁹T. J. Dunn, I. A. Walmsley, and S. Mukamel, *Phys. Rev. Lett.* **74**, 884 (1995).
- ³⁰M. Steffen, M. Ansmann, R. C. Bialczak, N. Katz, E. Lucero, R. McDermott, M. Neeley, E. M. Weig, A. N. Cleland, and J. M. Martinis, *Science* **313**, 1423 (2006).
- ³¹X. Li, T. Zhang, C. N. Borca, and S. T. Cundiff, *Phys. Rev. Lett.* **96**, 057406 (2006).
- ³²M. Aeschlimann, T. Brixner, A. Fischer, C. Kramer, P. Melchior, W. Pfeiffer, C. Schneider, C. Strüber, P. Tuchscherer, and D. V. Voronine, *Science* **333**, 1723 (2011).
- ³³J. Danckwerts, K. J. Ahn, J. Förstner, and A. Knorr, *Phys. Rev. B* **73**, 165318 (2006).
- ³⁴M.-R. Dachner, E. Malic, M. Richter, A. Carmele, J. Kabuss, A. Wilms, J.-E. Kim, G. Hartmann, J. Wolters, U. Bandelow, and A. Knorr, *Phys. Status Solidi B* **247**, 809 (2010).
- ³⁵M. Richter, K. J. Ahn, A. Knorr, A. Schliwa, D. Bimberg, M. E.-A. Madjet, and T. Renger, *Phys. Status Solidi B* **243**, 2302 (2006).
- ³⁶T. Unold, K. Mueller, C. Lienau, T. Elsaesser, and A. D. Wieck, *Phys. Rev. Lett.* **94**, 137404 (2005).
- ³⁷L. Jacak, P. Hawrylak, and A. Wójs, *Quantum Dots* (Springer, New York, 1998).
- ³⁸P. Borri, W. Langbein, S. Schneider, U. Woggon, R. L. Sellin, D. Ouyang, and D. Bimberg, *Phys. Rev. Lett.* **87**, 157401 (2001).
- ³⁹E. Stock, M.-R. Dachner, T. Warming, A. Schliwa, A. Lochmann, A. Hoffmann, A. I. Toropov, A. K. Bakarov, I. A. Derebezov, M. Richter, V. A. Haisler, A. Knorr, and D. Bimberg, *Phys. Rev. B* **83**, 041304 (2011).
- ⁴⁰M. Reichelt and T. Meier, *Opt. Lett.* **34**, 2900 (2009).
- ⁴¹S. Meyer and V. Engel, *Appl. Phys. B* **71**, 293 (2000).
- ⁴²P. Tian, D. Keusters, Y. Suzuki, and W. S. Warren, *Science* **300**, 1553 (2003).
- ⁴³D. Brinks, F. D. Stefani, F. Kulzer, R. Hildner, T. H. Taminiau, Y. Avlasevich, K. Müllen, and N. F. van Hulst, *Nature (London)* **465**, 905 (2010).
- ⁴⁴T. Brixner, F. J. G. de Abajo, J. Schneider, and W. Pfeiffer, *Phys. Rev. Lett.* **95**, 093901 (2005).
- ⁴⁵J. Pomplun, S. Burger, L. Zschiedrich, and F. Schmidt, *Phys. Status Solidi B* **244**, 3419 (2007).
- ⁴⁶L. Yang and S. Mukamel, *Phys. Rev. Lett.* **100**, 057402 (2008).
- ⁴⁷T. Kato and Y. Tanimura, *Chem. Phys. Lett.* **341**, 329 (2001).
- ⁴⁸T. Brixner, T. Mančal, I. V. Stiopkin, and G. R. Fleming, *J. Chem. Phys.* **121**, 4221 (2004).
- ⁴⁹T. Zhang, I. Kuznetsova, T. Meier, X. Li, R. P. Mirin, P. Thomas, and S. T. Cundiff, *Proc. Natl. Acad. Sci. USA* **104**, 14227 (2007).

⁵⁰X. Dai, M. Richter, H. Li, A. D. Bristow, C. Falvo, S. Mukamel, and S. T. Cundiff, *Phys. Rev. Lett.* **108**, 193201 (2012).

⁵¹The idea behind the filtering algorithm is that we can write the localized spectrum in terms of individual contributions $f_{e'}$ caused by resonances for different single excitons e' , where $f_{e'}$ are calculated from measured spectra [cf. Eq. (27)]:

$$S_{k_{III}}(i, \Omega_1, \Omega_2, t_3) = \sum_{e'} c_i^{e'^*} \mu_{ig}^* \cdot E_i^1(\mathbf{r}_i, \omega_{eg}) f_{e'}(\Omega_1, \Omega_2, t_3). \quad (28)$$

Multiplying the equation with c_i^e and summing over i yields a scalar product, and we get $f_{e'}$ defined using the localized spectra

[Eq. (27)]. The far-field double-quantum-coherence spectrum can also be calculated using $f_{e'}$:

$$S_{k_{III}}(\Omega_1, \Omega_2, t_3) = \sum_{e'} c_i^{e'^*} \mu_{ig}^* \cdot E^1(\omega_{eg}) f_{e'}(\Omega_1, \Omega_2, t_3). \quad (29)$$

It is expressed using summands for every contributing single exciton e' , and the summand of the exciton to be filtered can be subtracted. This is possible, since every summand can be calculated using $f_{e'}$, which can be calculated from the experimental data of the localized spectrum, if the expansion coefficients of the single-exciton wave function of e' are known.